

pubs.acs.org/acsaelm Article

Beta to Spinel Phase Transition of Magnesium Gallium Oxide Thin Films and Their Photoluminescence Properties

Tianchen Yang, Chengyun Shou, Abdullah Almujtabi, Quazi Sanjid Mahmud, Edward Zhu, Yuan Li, and Jianlin Liu*



Cite This: ACS Appl. Electron. Mater. 2024, 6, 6640-6647



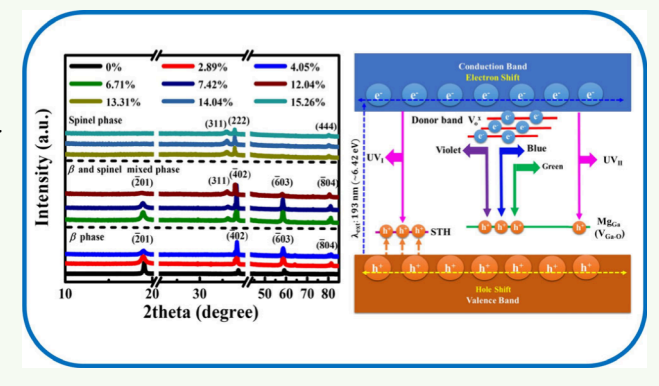
ACCESS I

III Metrics & More

Article Recommendations

sı Supporting Information

ABSTRACT: As a promising Ga_2O_3 -based ultrawide bandgap semiconductor, beta (β) phase and spinel phase magnesium gallium oxide (MgGaO) with tunable bandgap larger than 4.8 eV has great potential in power electronics and deep ultraviolet optoelectronics. However, the role of Mg composition on the phase transition of MgGaO thin films from the β to spinel phase and their photoluminescence (PL) properties are still not explored. In this perspective, nine MgGaO samples with Mg atomic percent from 0 to 15.26% were grown by using oxygen plasma assisted molecular beam epitaxy. Bandgap tuning from 4.86 to 5.45 eV in MgGaO alloys was observed. The phase transition between β -MgGaO and spinel MgGa₂O₄ thin films was confirmed, and lattice parameters changing with Mg at. % were extracted by X-ray diffraction theta/2theta scans and in plane reciprocal space mapping. Room temperatures, power.



and in-plane reciprocal space mapping. Room temperature-, power-, and temperature-dependent PL properties of these MgGaO films were investigated, and the PL mechanisms were revealed.

KEYWORDS: magnesium gallium oxide, phase transition, photoluminescence, molecular beam epitaxy, ultrawide bandgap semiconductor

■ INTRODUCTION

As one of the most promising ultrawide bandgap (UWBG) semiconductor materials, β -Ga₂O₃ has gained significant popularity in high-performance power electronic and optoelectronic devices. 1-3 The critical electric field of ~8 MV/cm allows for its applications in high-power diodes and field-effect transistors.4-6 Additionally, its large bandgap energy enables deep ultraviolet (UV) optoelectronic device applications.^{7,8} To extend the applications of Ga2O3-based devices beyond the beta phase structure, bandgap engineering through Mg incorporation is highly desirable. 9-13 Both amorphous MgGaO^{9,10} and β -MgGaO^{11,13} have been reported for deep-UV photodetector applications. Previously, we confirmed that the MgGaO lattice structure transforms from beta phase to beta and rocksalt mixed phase, and finally to rocksalt phase, as the normalized cations Mg at.%/Ga at.% change from 0%/ 100% to 100%/0%. 12 However, the interval of Mg and Ga composition change in the above study was a bit too big; normalized cations Mg at.%/Ga at.% were not tuned to be around 33.33%/66.67%, which could lead to the spinel MgGa₂O₄ phase, a promising transparent semiconducting oxide 14,15 for optoelectronic and power electronic applications. 16 In addition, carefully tuning Mg compositions within 33.33% in MgGaO may lead to a transition between β -phase and spinel phase, which was not explored in the previous study¹² and remains unknown. Furthermore, there is a lack of comprehensive photoluminescence (PL) studies of $\beta\text{-MgGaO}$ and spinel MgGa₂O₄ thin films, although several room-temperature $^{17-20}$ and a few temperature-dependent 21 PL studies of Mg-doped $\beta\text{-Ga}_2\text{O}_3$ were conducted, and preliminary room-temperature PL studies of MgGa₂O₄ were reported. 22,23

To refine the phase transition conditions from β -MgGaO to spinel MgGa₂O₄ and to investigate the PL mechanism of MgGaO films with varying Mg atomic percentages, this study involves the growth of nine MgGaO thin film samples with Mg atomic percentages ranging from 0 to 15.26% (normalized across all Mg, Ga, and O elements in the alloys) using plasma-assisted molecular beam epitaxy (MBE). The structural transformation, film quality, lattice parameters, optical bandgap, and transmittance properties were examined. Additionally, comprehensive PL studies of these MgGaO thin films, including power- and temperature-dependent PL measurements, were carried out.

Received: June 17, 2024 Revised: August 22, 2024 Accepted: August 22, 2024 Published: August 29, 2024





Table 1. Characterized Parameters of Nine MgGaO Thin Films with Mg Atom % from 0% to 15.26%

		Relative atomic percent (EDX)					
Sample index	Film thickness (nm)	Mg %	Ga %	O %	Chemical formula	Phase identification	Bandgap (eV)
#1	364.35	0	40.05	59.95	Ga_2O_3	β -phase	5.02
#2	379.97	2.89	37.28	59.83	$(Mg_{0.07}Ga_{0.93})_2O_3$	β -phase	5.08
#3	397.01	4.05	35.84	60.10	$(Mg_{0.1}Ga_{0.9})_2O_3$	β -phase	5.11
#4	665.70	6.71	33.93	59.36	$Mg_{0.067}Ga_{0.339}O_{0.594}$	Mixed phase	4.86
#5	744.52	7.42	33.45	59.13	$Mg_{0.074}Ga_{0.335}O_{0.591}$	Mixed phase	4.88
#6	1319.69	12.04	30.24	57.72	$Mg_{0.12}Ga_{0.30}O_{0.58}$	Mixed phase	5.35
#7	1137.10	13.31	28.91	57.78	$Mg_{0.92}Ga_{2.00}O_4$	Spinel phase	5.38
#8	1224.85	14.04	28.44	57.52	$Mg_{0.97}Ga_{1.98}O_4$	Spinel phase	5.43
#9	1203.95	15.26	27.71	57.03	$Mg_{1.07}Ga_{1.94}O_{4} \\$	Spinel phase	5.45

■ EXPERIMENTAL SECTION

Film Growth. An SVT Associates MBE system with a base pressure of 10⁻⁹ Torr was used to grow MgGaO samples. Two-inch cplane sapphire wafers were used as substrates. The substrate was cleaned by using a piranha solution $(H_2O_2:H_2SO_4 = 3:5)$ at 200 °C for approximately 20 min. Subsequently, the substrate was rinsed in deionized water, blown dry with a nitrogen gun, and transferred to the MBE load-lock chamber. After the pressure of the load-lock chamber was reduced more than approximately 10⁻⁶ Torr, the substrate was finally transferred to the substrate holder in the main chamber. The substrate temperature was raised by a heater placed behind the substrate, and a pregrowth substrate annealing process was conducted at 800 °C for 20 min. The substrate temperature was then reduced to 600 °C for sample growth. During the growth, oxygen was introduced at a rate of 2.0 sccm using an RF plasma at 400 W. The elemental high-purity Ga (6 N) effusion cell temperature was maintained at 750 °C, and the Mg (4 N) effusion cell temperature was varied from 390 to 423 °C, resulting in the growth of nine MgGaO thin film samples with different Mg atomic percentages. The growth for each sample lasted 5 h. Following growth, a postannealing process was conducted at 700 °C for 20 min without an oxygen atmosphere.

Film Characterization. The film thickness of the samples, as listed in Table 1, was measured by using a Veeco Dektak 8 profilometer. The relative atomic ratios of Mg, Ga, and O in all samples were determined by energy-dispersive X-ray (EDX) analysis using a TESCAN Vega3 SBH scanning electron microscope (SEM). The film structure, quality, and lattice parameters were characterized by X-ray diffraction (XRD) techniques, including theta/2theta scans, rocking curves, in-plane phi scans, and reciprocal space mapping (RSM), using a Bruker D8 Advance X-ray diffractometer and a Rigaku SmartLab X-ray diffractometer with Cu K α radiation (λ = 1.5405 Å) at room temperature. Absorption and transmittance spectra were measured at room temperature with a high-performance UV-vis-NIR spectrophotometer (Cary 5000, Agilent Inc.). Power- and temperature-dependent PL spectra were obtained using a custombuilt PL system equipped with a 193 nm ArF excimer laser (Coherent Inc.) and a helium compressor (SHI-APD Cryogenics Inc.). The laser, operating in constant energy mode, allowed for varying incident power densities by adjusting the energy values of the beam through a constant beam area defined by the beam slit. Temperature control of PL from 14 to 300 K was used.

RESULTS AND DISCUSSION

Figure 1 shows the EDX spectra of all MgGaO thin films. The O K α , Ga L α , and Mg K α peaks are located at approximately 0.525, 1.098, and 1.253 keV, ^{12,13,15} respectively. Due to the substantial film thickness, the Al signal from the substrate is undetectable. Based on the integrated area of the peaks, the elemental compositions are obtained as listed in Table 1. The Mg at.% increases monotonically from 0% to 15.26% across samples #1 to #9.

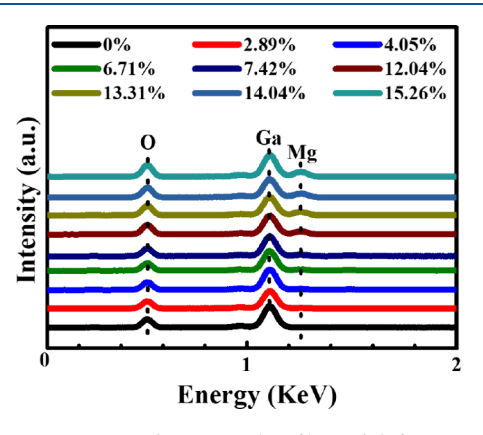


Figure 1. EDX spectra of MgGaO thin films of different Mg atomic percent.

Figure 2(a) depicts the schematics of lattice structures of β -MgGaO and spinel MgGa₂O₄ grown on a c-sapphire substrate, where the β -phase $\{\overline{201}\}$ planes and spinel phase $\{111\}$ planes epitaxially align along the *c*-sapphire [0001] orientation. Figure 2(b) shows the XRD pattern of all MgGaO samples obtained through theta/2theta scanning. Samples #1-#3, with Mg atomic percentages ranging from 0 to 4.05%, exhibit pure β phase. According to Ga₂O₃ PDF 01-087-1901, four distinct diffraction peaks are observed at approximately 19.12°, 38.50°, 59.14°, and 82.37°, corresponding to the β -phase ($\overline{2}01$), ($\overline{4}02$), $(\overline{603})$, and $(\overline{804})$, $(\overline{804})$, respectively, indicating a clear monoclinic structure. The chemical formula for films in the β -phase can be expressed as $(Mg_xGa_{1-x})_2O_3$ (Table 1). Taking sample no. 2 as an example, its formula can be expressed as (Mg_{0.07}Ga_{0.93})₂O₃. On the other hand, according to MgGa₂O₄ PDF 00-010-0133, samples #7-#9, with Mg atomic percentages between 13.31% and 15.26%, display a pure spinel phase with diffraction peaks at approximately 35.93°, 37.59°, and 80.24°, corresponding to the spinel phase (311), (222), and (444), ^{27,28} respectively. The existence of (222) and (444) but lack of (111) and (333) diffraction peaks is noticed, which may be due to unsubstantiated destructive interference of the latter planes. The chemical formula for films in spinel phase can be expressed as $Mg_xGa_vO_4$, where x and y are close to 1 and 2, respectively (Table 1). For example, the chemical formula of sample #9 can be expressed as ~Mg_{1.07}Ga_{1.94}O₄. Samples #4– #6, with Mg atomic percentages from 6.71% to 12.04%, exhibit a mixed phase of β and spinel, as evidenced by the presence of both β -phase ($\overline{201}$), ($\overline{402}$), ($\overline{603}$), and ($\overline{804}$) peaks and the spinel phase (311) peak in the XRD pattern. The chemical formula in this region can be expressed as Mg_xGa_yO_z (Table 1). For example, the chemical formula of sample #6 can be

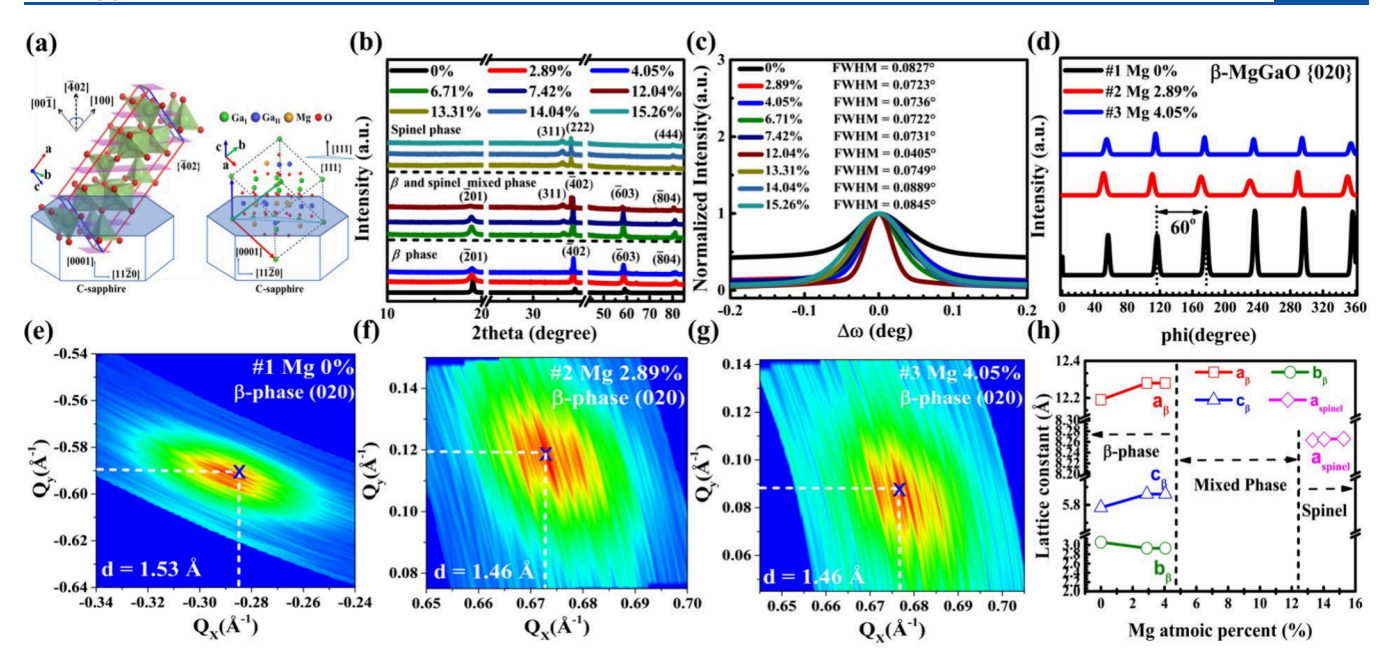


Figure 2. (a) Schematic of lattice structures of MgGaO films in both β - and spinel phases grown on c-sapphire. (b) XRD patterns of MgGaO films with various Mg atomic percentages in theta-2theta scans. (c) Normalized XRD rocking curves. (d) φ -scan patterns of the β -MgGaO {020} plane. (e-g) In-plane RSM of samples #1-#3 of the β -phase (020). (h) β -phase lattice constant a_{β} , b_{β} , c_{β} and spinel phase lattice constant a_{spinel} versus Mg atomic percentage.

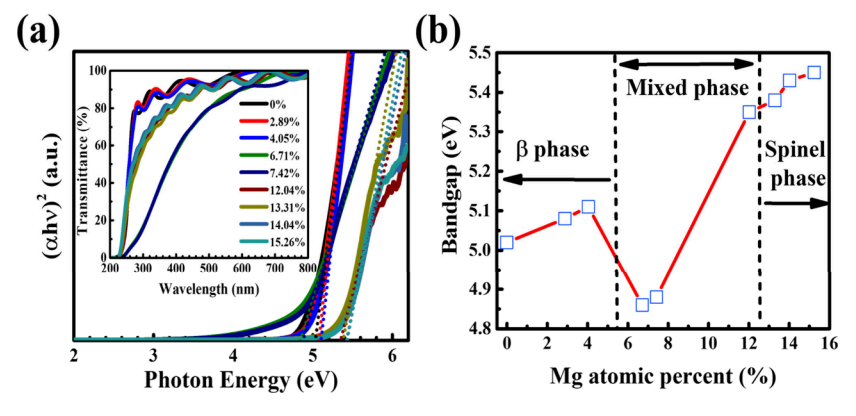


Figure 3. (a) Tauc plot absorption spectra, with an inset showing the corresponding transmittance spectra. (b) The relationship between the bandgap and Mg atomic percentage across various MgGaO samples.

written as $Mg_{0.12}Ga_{0.30}O_{0.58}$. Furthermore, as the Mgcomposition increases, the diffraction angles decrease due to the larger ionic radius of Mg (0.72 Å) compared to Ga (0.62 Å) in both β - and mixed phases. ^{12,13,29} The 2theta positions of the (402) peak for the β -phase and mixed phase, as well as the (222) peak for the spinel phase, are summarized in Table S1 in the Supporting Information. Figure 2(c) shows normalized XRD rocking curves of (402) and (222) peaks for β -phase and β /spinel mixed phase and spinel phase samples, respectively. The full width at half-maximum (fwhm) values for β -phase samples #1-#3 are 0.0827°, 0.0732°, and 0.0736°; for mixed phase samples #4–#6, they are 0.0722° , 0.0731° , and 0.0405° ; and for spinel samples #7-#9, they are 0.0749°, 0.0889°, and 0.0845°, respectively. These low fwhm values indicate the high quality of our films. ^{12,13} Given the single-phase nature of β phase films, Figure 2(d) shows β -MgGaO {020} φ -scan patterns for samples #1-#3 at a 2theta_chi detector position of 60.961° (PDF 01-087-1901). Consistent with previously reported β -Ga₂O₃^{30,31} and β -MgGaO¹² {020} φ -scan patterns, all three films exhibit a 6-fold rotational symmetry.

Lattice constants a_{β} and c_{β} of β -phase samples can be obtained from the XRD pattern in theta/2thta scan mode in Figure 2(b), while b_{β} of these β -phase samples were obtained by in-plane reciprocal space mapping of the β -phase (020) plane, which are shown in Figures 2(e)–(g), respectively. Specifically, we derived the interplanar distance $d_{(402)}^-$ of the β -phase samples by applying Bragg's law. Then, we utilized established equations from prior studies $d_{(402)}^-$ to calculate the lattice constants d_{β} and $d_{(620)}^-$ From RSM results in Figures 2(e)–(g), the interplanar distance $d_{(620)}^-$ is obtained by the formula $d_{(620)}^- = \frac{1}{\sqrt{R_x^2 + R_y^2}}$, where $d_{(620)}^-$ are coordinate values of $d_{(620)}^-$

and Q_y in reciprocal space, from which the lattice constant b_β of β -phase samples is calculated as twice $d_{(020)}$. Similarly, we obtained the interplanar distance $d_{(222)}$ for the pure spinel samples from XRD theta/2theta scan patterns, enabling the calculation of the lattice constant a_{spinel} as $2\sqrt{3} d_{(222)}$. These lattice constant values are listed in Table S1 in the Supporting Information. Figure 2(h) shows the lattice constants as a

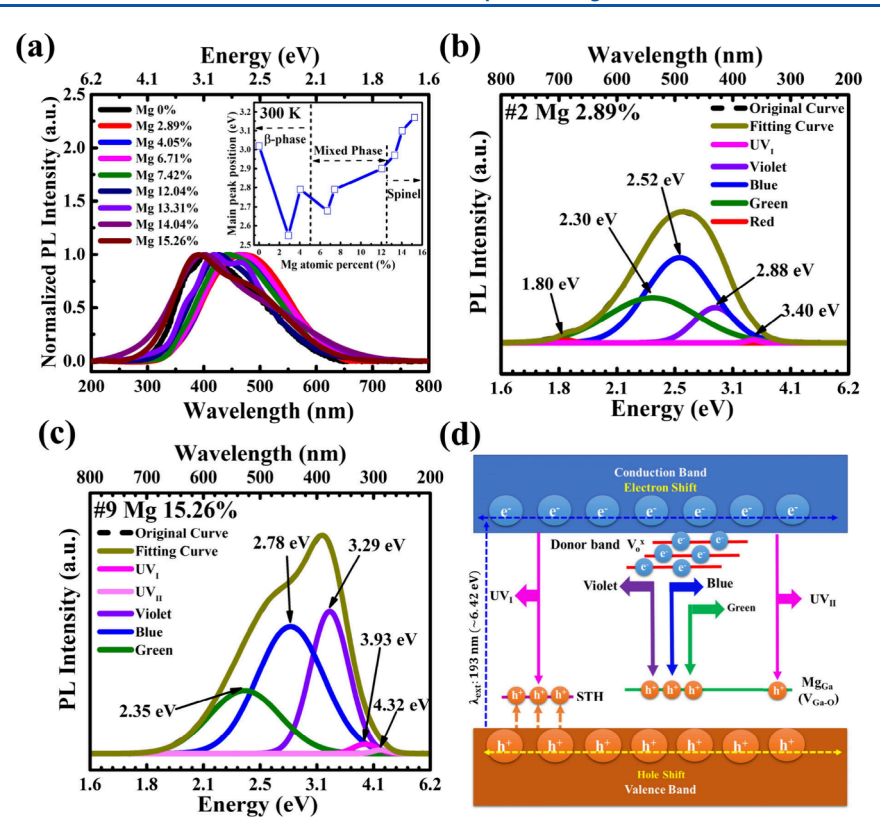


Figure 4. (a) Normalized PL spectra of all samples at room temperature (the inset is the PL main peak position versus Mg atomic percent). (b, c) PL deconvolution for sample #2 in beta phase and #9 in spinel phase, respectively. (d) Schematic energy level diagram illustrating optical transitions in both beta and spinel MgGaO.

Table 2. Main PL Peak Position and the Spatial Distribution of Defect Levels in Undoped β -Ga₂O₃, β -MgGaO, β , and Spinel Mixed Phase and Spinel MgGaO at Room Temperature^a

MgGaO sample	Main PL peak position at RT (eV)	$V_{O_I}(\mathrm{eV})$	$V_{O_{II}}(\mathrm{eV})$	$V_{O_{III}}(\mathrm{eV})$	$E_{STH}^{bind}(\mathrm{eV})$	$Mg_{Ga}(V_{Ga-O})$ (eV)
#1 Mg 0%	3.02	1.32	2.04	1.8	0.49	(0.63)
#2 Mg 2.89%	2.55	1.51	2.09	1.87	0.58	(0.69)
#3 Mg 4.05%	2.79	-	-	-	0.51	-
#4 Mg 6.71%	2.68	-	-	-	0.40	-
#5 Mg 7.42%	2.79	-	-	-	0.42	-
#6 Mg 12.04%	2.90	-	-	-	0.78	-
#7 Mg 13.31%	2.97	0.68	1.17	1.05	0.89	1.69
#8 Mg 14.04%	3.10	1.02	2.05	1.57	0.61	1.21
#9 Mg 15.26%	3.17	1.03	1.97	1.54	0.42	1.13
β -Ga ₂ O ₃ ^{35,36}	2.5-3.0	1.38	1.76	1.56	0.53	(0.27)
$Mg:Ga_2O_3^{21,35,37}$	1.5-2.5	1.44	1.77	1.61	-	1.0 - 1.5(0.35)
DFT ¹⁸	-	1.6	2.0	1.7	-	1.05

"Specifically, these values are referenced to the energy (in eV) below the conduction band minimum (CBM) for oxygen vacancies associated with donor bands and above the valence band maximum (VBM) for self-trapped holes (STHs) and V_{Ga-O} and Mg_{Ga} acceptors. Corresponding experimental and density functional theory (DFT) calculated values of β -Ga₂O₃ and Mg-doped Ga₂O₃ from the literature are included for comparison.

function of the Mg atomic percentage. In β -phase MgGaO samples, both a_{β} and c_{β} increase, while b_{β} decreases with increasing Mg at.%, compared to the reference values of β -Ga₂O₃, which are approximately 12.20 Å, 5.799 Å, and 3.04 Å, respectively (β -Ga₂O₃ PDF 01-087-1901). In spinel phase MgGa₂O₄ samples, the lattice constant $a_{\rm spinel}$ shows a slight increase with the increase of the Mg atomic percentage, compared with a reference value of approximately 8.288 Å (MgGa₂O₄ PDF 00-010-0133).

Figure 3(a) shows absorption spectra of all samples in the Tauc plot. Both β -MgGaO^{11-13,32,33} and spinel

 ${\rm MgGa_2O_4^{14,15,34}}$ were acknowledged as direct bandgap semiconductors. Implicit in this analysis is the assumption that their ternary alloy, the mixed phase MgGaO, likewise conforms to this intrinsic property. Employing the Tauc equation $(\alpha hv)^2 = A(hv - E_g)$, wherein hv signifies energy, α denotes the absorption coefficient, and A represents a constant, the bandgap E_g is discerned. This determination involved extrapolating the linear portion of the absorption spectra to intersect the hv-axis through linear regression, as documented in Table 1 of the Supporting Information. The inset of Figure 3(a) shows transmittance spectra, manifesting a discernible reduction in light transmittance from approximately 90% in the beta phase to a range of 60-80% in the mixed phase, followed by an ascent to approximately 80% in the spinel phase, spanning the visible spectrum. Figure 3(b) shows a graphical representation of the bandgap modulation with varying Mg composition in MgGaO films. It is noted that the bandgap exhibits a consistent augmentation with escalating Mg atomic percentages in both the beta phase and the transition from mixed to spinel phases. Nevertheless, a conspicuous decline in bandgap transpires from the beta to the mixed phase, ostensibly attributed to the abrupt emergence of the spinel phase characterized by a diminished bandgap. This decline, from 5.11 to 4.86 eV, underscores the discernible influence of the spinel phase in attenuating the comparatively larger bandgap intrinsic to the beta phase.

Figure 4(a) shows normalized room temperature (RT) PL spectra of all samples, which were acquired at an incident power density of 12.8 mW/cm². Analogous to RT PL spectra observed in Mg-doped β -Ga₂O₃, ^{18,20,21,38} the spectra display broad luminescence, with the primary peak reaching maximum intensity within the 300-600 nm range. The main PL peak positions are listed in Table 2. Correspondingly, the inset in Figure 4(a) shows the main PL peak positions as a function of the Mg atomic percentage. The main PL peak position of sample #1 is located at ~3.02 eV (~409.99 nm), which is in good agreement with the reported main PL peak position of bulk β -Ga₂O₃ at ~3.10 eV (~400 nm). After incorporating Mg, the main PL peak position of the beta phase MgGaO films decreases below 3.0 eV. A similar phenomenon was observed with the main PL peak of a Mg-doped β -Ga₂O₃ single crystal at ~2.75 eV (~450 nm) with respect to ~2.95 (~420 nm) of its undoped β -Ga₂O₃. In addition, all main PL peaks manifest a blue shift among MgGaO thin films as the Mg composition increases, which is consistent with the escalating optical bandgap observed in β -MgGaO, mixed phase, and spinel phase regions, respectively. RT PL peak deconvolution was conducted to discern the optical transitions within all samples. As illustrated by sample no. 2 in the beta phase and sample no. 9 in the spinel phase here, Figure 4(b) shows the deconvoluted PL peaks for sample no. 2, encompassing emissions at approximately 3.40 eV for UV_I emission, 2.88 eV for violet, 2.52 eV for blue, 2.30 eV for green, and 1.80 eV for red. Meanwhile, Figure 4(c) shows the deconvoluted PL peaks for sample #9, revealing emissions at around 3.93 eV for UV_I, 4.32 eV for UV_{II}, 3.29 eV for violet, 2.78 eV for blue, and 2.35 eV for green. PL deconvolution for all remaining samples is shown in Figure S1 in the Supporting Information.

The energy level diagram outlining the PL mechanism in both β -MgGaO and spinel MgGa₂O₄ films is depicted in Figure 4(d). Similar to the energy levels predicted or observed in β -Ga₂O₃, Mg-doped Ga₂O₃, and spinel MgGa₂O₄ thin films, ^{18,21,23} three oxygen-vacancy-related donor levels, polaronic self-trapped hole (STH) states, Mg on a Ga site (Mg_{Ga}) acceptor level, or Ga and O vacancy defect complex acceptor level (V_{Ga-O}), are included in addition to the conduction and valence bands. The UV₁ emission observed in all films is attributed to the optical transition between the electrons in the conduction band and the STHs. Its energy E_{UV_1} can be calculated based on the equation $E_{UV_1} = E_g - E_{polaron}^{STH} - E_{STH}^{bind}$, where E_g is the bandgap, $E_{polaron}^{STH}$ is the polaronic STH energy level of ~1.1 eV above the valence band, which is assumed to

be the same as in β -Ga₂O₃, ¹⁸ and E_{STH}^{bind} is the binding energy of STHs to an oxygen atom. E_{STH}^{bind} for all samples were calculated and are summarized in Table 2. For example, E_{STH}^{bind} of pure β -phase sample #2 and pure spinel sample #9 is estimated to be ~0.58 and 0.42 eV, respectively, which is close to ~ 0.53 eV of β -Ga₂O₃³⁶ The second UV peak (UV_{II}), which is attributed to an optical transition between conduction band and MgGa antisite acceptors in MgGaO thin films or VGa-O defect complex acceptors in the Ga2O3 reference sample, can be extracted. 35,44,45 The difference is that this peak can be observed at room temperature for pure spinel MgGa₂O₄ samples, as shown in Figure 4(c), while it can be revealed only at low temperature for Ga_2O_3 and low-Mg composition β -MgGaO thin films, as shown later. The acceptor ionization energies E_{A} (either $E_{Mg_{Ga}}$ or $E_{V_{Ga-O}}$) of these samples can be calculated as $E_A = E_g - E_{UV_{II}}$ and are listed in Table 2. As shown in the table, the acceptor ionization energies for β - Ga_2O_3 and β -MgGaO sample 2 are 0.63 and 0.69 eV, respectively. The high similarity of these values suggests that the acceptor responsible for the UV_{II} optical transition in β -MgGaO sample 2 could still be dominated by V_{Ga-O} instead of Mg_{Ga} antisite acceptors even if almost 2.9 at.% Mg is incorporated in the alloy. Nevertheless, these values are larger than reported V_{Ga-O} acceptor ionization energies in β -Ga₂O₃ and Mg-doped Ga₂O₃ samples, which may be due to the smaller bandgaps of their samples. On the other hand, the acceptor ionization energies are ~1.69, 1.21, and 1.13 eV for pure spinel MgGa₂O₄ samples 7-9, respectively. It is noted that the acceptor ionization energy decreases with increasing Mg atomic percent; namely, it shifts toward the valence band maximum (VBM) as the Mg composition increases in these spinel samples. In comparison, the Mg_{Ga} deep acceptor energy level of Mg-doped β -Ga₂O₃ was determined experimentally at ~1.79 eV above the valence band edge,²¹ while calculated Mg_{Ga} energy levels are appropriately situated in the range of 1–1.5 eV above the VBM.²¹ Since the acceptor ionization energies are similar to these reported values, it can be inferred that Mg_{Ga} antisite species are the dominating deep acceptors in MgGa₂O₄ spinel samples.

Besides the above UV emissions, violet, blue, and green visible emissions were observed for all films, which originate from donor-acceptor pair (DAP) transitions between three oxygen vacancy donor bands and V_{Ga-O} acceptor bands or Mg_{Ga} antisite acceptor levels, as shown in Figure 4(d). Using these visible emission peak energies, with a knowledge of the acceptor energy level, the three oxygen vacancy level positions can be calculated, or vice versa. Table 2 lists these values that can be extracted. For example, the three oxygen vacancy levels for Ga₂O₃ sample #1 are estimated at 1.32, 1.8, and 2.04 eV below the conduction band edge, which is in good agreement with DFT calculation results of 1.6, 1.7, and 2.0 eV, 18 respectively. For β -phase MgGaO sample #2, the oxygen vacancy energy levels are estimated at 1.51, 1.87, and 2.09 eV below the conduction band edge, respectively. The estimated energy levels of the three oxygen vacancies of spinel sample no. 9 are 0.98, 1.49, and 1.92 eV below the conduction band edge, respectively. Since there were no UVII peaks detected in sample #3 and mixed-phased samples, the oxygen vacancy energy levels cannot be calculated. Finally, a very weak red emission located at ~680 nm was observed for MgGaO samples #2-#6 in the beta and mixed phases, which is similar

to the reported \sim 690 nm red emission in Mg-doped β -Ga₂O₃. The origin of the red emission remains unclear, although it was suggested to be a transition between valence band and Mg_{Ga} antisite deep acceptor energy levels. ²¹

Figure 5(a),(b) show power-dependent PL spectra of β -MgGaO sample #2 and spinel MgGa₂O₄ sample #9 at 14 K,

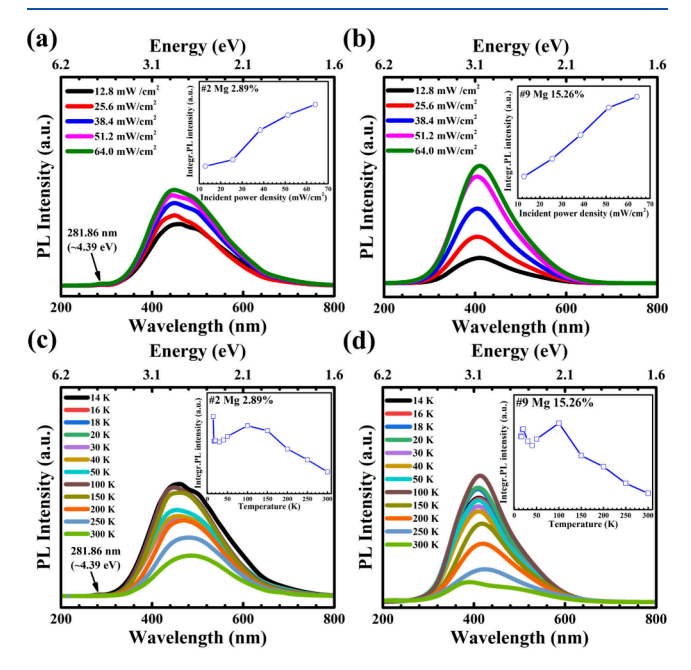


Figure 5. (a, b) Power-dependent PL spectra at 14 K for sample #2 and #9. Insets are the integrated PL intensity versus incident power density, respectively. (c, d) Temperature-dependent PL spectra at 12.8 mW/cm² for samples #2 and #9. Insets are the integrated PL intensity versus temperature, respectively.

with excitation power densities ranging from 12.8 to 64.0 mW/ cm², respectively, and the insets are the integrated PL intensity versus power density accordingly. The corresponding results for the remaining samples are provided in Figures S2(a)-(g)in the Supporting Information. For each sample, the PL peak position remains stable despite variations in the incident power density. In addition, the increase in integrated PL intensity with increasing incident power density is attributed to the increased number of pumped electrons, following a similar nonlinear trend. 46,47 This behavior is indicative of the interplay among Shockley-Read-Hall (SRH) recombination, spontaneous emission, and Auger recombination processes.⁴⁷ It should also be noted that a UV peak, which is designated as UV_{II} emission, emerges at approximately 4.39 eV at 14 K for both β -Ga₂O₃ sample #1 (Figure S2(a)) and β -MgGaO sample #2 (Figure 5(a)). This UV_{II} emission is attributed to the recombination of electrons in the conduction band and holes in the V_{Ga-O} defect complex acceptor level in Ga_2O_3 and/or the MgGa antisite acceptor level in MgGaO, as discussed earlier.

Figures S(c),(d) show temperature-dependent PL spectra of samples #2 and #9, recorded over a temperature range between 14 and 300 K with an incident lasing power density of 12.8 mW/cm², respectively. The inset is the integrated PL intensity versus temperature accordingly. The corresponding results for the remaining samples are shown in Figures S3(a)-(g) in the Supporting Information. Across all samples, the PL exhibits negative thermal quenching (NTQ) effects for the temperature

below $\sim \! 100$ K, while positive thermal quenching (PTQ) effects dominate with the temperature above $\sim \! 100$ K. The PTQ is primarily due to the fact that thermal energy promotes nonradiative recombination pathways such as SRH recombination. On the other hand, the existence of NTQ suggests the presence of multiple intermediate energy levels within the bandgap that participate in radiative recombination processes, which is the case in our samples.

CONCLUSION

In this study, we conducted the growth of nine MgGaO thin films via MBE, with varying Mg atomic percentages spanning from 0 to 15.26%. Our primary focus was to elucidate the phase transition phenomena from the β -phase to the spinel phase and PL properties of these films. Through systematic investigation, we established distinct phase boundaries: when the Mg atomic percentage ranges from 0 to 4.05%, the material predominantly exhibits pure β -phase; within the Mg atomic percentage range of 6.71% to 12.04%, a mixture of β -phase and spinel phase is observed; while at Mg atomic percentages between 13.31% and 15.26%, the material transitions entirely into pure spinel phase. Comprehensive PL studies were carried out, unraveling the PL mechanisms associated with both β -MgGaO and spinel MgGa2O4 thin films. Our investigation contributes to a deeper understanding of the intricate phase transitions and sheds light on the defect energy levels intrinsic to Ga₂O₃-based MgGaO alloys. This elucidation holds promise for optimizing the performance of UWBG semiconductor electronic and optoelectronic devices through informed design strategies based on a thorough comprehension of the crystal structure and defect characteristics.

ASSOCIATED CONTENT

Supporting Information

The Supporting Information is available free of charge at https://pubs.acs.org/doi/10.1021/acsaelm.4c01079.

Characterized parameters of nine MgGaO thin films; XRD peak position, *d*-spacing, lattice constant of MgGaO thin films in beta, mixed, and spinel phase; room-temperature PL deconvolution; power-dependent PL and integrated PL intensity versus incident power density; temperature-dependent PL and integrated PL intensity versus temperature (PDF)

AUTHOR INFORMATION

Corresponding Author

Jianlin Liu — Department of Electrical and Computer Engineering, University of California, Riverside, California 92521, United States; ⊚ orcid.org/0000-0001-6513-0867; Phone: 1-9518277131; Email: jianlin@ece.ucr.edu; Fax: 1-9518272425

Authors

Tianchen Yang — Department of Electrical and Computer Engineering, University of California, Riverside, California 92521, United States; ⊚ orcid.org/0000-0002-0991-471X

Chengyun Shou — Department of Electrical and Computer Engineering, University of California, Riverside, California 92521, United States

Abdullah Almujtabi — Department of Electrical and Computer Engineering, University of California, Riverside, California 92521, United States

- Quazi Sanjid Mahmud Department of Electrical and Computer Engineering, University of California, Riverside, California 92521, United States
- Edward Zhu Department of Electrical and Computer Engineering, University of California, Riverside, California 92521, United States
- Yuan Li Department of Electrical and Computer Engineering, University of California, Riverside, California 92521, United States

Complete contact information is available at: https://pubs.acs.org/10.1021/acsaelm.4c01079

Notes

The authors declare no competing financial interest.

ACKNOWLEDGMENTS

This work was supported by the National Science Foundation (ECCS-2105566) and the Air Force Office of Scientific Research under DURIP award number FA9550-22-1-0505. The authors acknowledge the use of facilities and instrumentation at the UC Irvine Materials Research Institute (IMRI), which is supported in part by the National Science Foundation through the UC Irvine Materials Research Science and Engineering Center (DMR-2011967).

REFERENCES

- (1) Tsao, J. Y.; Chowdhury, S.; Hollis, M. A.; Jena, D.; Johnson, N. M.; Jones, K. A.; Kaplar, R. J.; Rajan, S.; Van de Walle, C. G.; Bellotti, E.; Chua, C. L.; Collazo, R.; Coltrin, M. E.; Cooper, J. A.; Evans, K. R.; Graham, S.; Grotjohn, T. A.; Heller, E. R.; Higashiwaki, M.; Islam, M. S.; Juodawlkis, P. W.; Khan, M. A.; Koehler, A. D.; Leach, J. H.; Mishra, U. K.; Nemanich, R. J.; Pilawa-Podgurski, R. C. N.; Shealy, J. B.; Sitar, Z.; Tadjer, M. J.; Witulski, A. F.; Wraback, M.; Simmons, J. A. Ultrawide-Bandgap Semiconductors: Research Opportunities and Challenges. *Advanced Electronic Materials* **2018**, 4 (1), 1600501.
- (2) Xie, C.; Lu, X.-T.; Tong, X.-W.; Zhang, Z.-X.; Liang, F.-X.; Liang, L.; Luo, L.-B.; Wu, Y.-C. Recent Progress in Solar-Blind Deep-Ultraviolet Photodetectors Based on Inorganic Ultrawide Bandgap Semiconductors. *Adv. Funct. Mater.* **2019**, 29 (9), 1806006.
- (3) Kim, M.; Seo, J.-H.; Singisetti, U.; Ma, Z. Recent Advances in Free-Standing Single Crystalline Wide Band-Gap Semiconductors and Their Applications: GaN, SiC, ZnO, β -Ga₂O₃, and Diamond. *Journal of Materials Chemistry C* **2017**, 5 (33), 8338–8354.
- (4) Pearton, S. J.; Yang, J.; Cary, P. H.; Ren, F.; Kim, J.; Tadjer, M. J.; Mastro, M. A. A Review of Ga₂O₃ Materials, Processing, and Devices. *Applied Physics Reviews* **2018**, 5 (1), 011301.
- (5) Sharma, S.; Zeng, K.; Saha, S.; Singisetti, U. Field-Plated Lateral Ga₂O₃ MOSFETs With Polymer Passivation and 8.03 kV Breakdown Voltage. *IEEE Electron Device Lett.* **2020**, *41* (6), 836–839.
- (6) Zeng, K.; Vaidya, A.; Singisetti, U. 1.85 kV Breakdown Voltage in Lateral Field-Plated Ga₂O₃ MOSFETs. *IEEE Electron Device Lett.* **2018**, 39 (9), 1385–1388.
- (7) Oh, S.; Kim, C.-K.; Kim, J. High Responsivity β -Ga₂O₃ Metal-Semiconductor-Metal Solar-Blind Photodetectors with Ultraviolet Transparent Graphene Electrodes. *ACS Photonics* **2018**, 5 (3), 1123–1128
- (8) Chen, X.; Ren, F.; Gu, S.; Ye, J. Review of Gallium-Oxide-Based Solar-Blind Ultraviolet Photodetectors. *Photon. Res., PRJ.* **2019**, 7 (4), 381–415.
- (9) Xu, C.; Du, Z.; Huang, Y.; Dong, M.; Lin, R.; Li, Y.; Wang, B.; Zheng, W.; Huang, F. Amorphous-MgGaO Film Combined with Graphene for Vacuum-Ultraviolet Photovoltaic Detector. *ACS Appl. Mater. Interfaces* **2018**, *10* (49), 42681–42687.
- (10) Dong, M.; Zheng, W.; Xu, C.; Lin, R.; Zhang, D.; Zhang, Z.; Huang, F. Ultrawide-Bandgap Amorphous MgGaO: Nonequilibrium

- Growth and Vacuum Ultraviolet Application. Advanced Optical Materials 2019, 7 (3), 1801272.
- (11) Shou, C.; Yang, T.; Almujtabi, A.; Yang, T.; Li, Y.; Mahmud, Q. S.; Xu, M.; Zheng, J.-G.; Liu, J. Improving Crystal Quality of β -Phase MgGaO Thin Films by Using Low-Temperature Homo-Buffer Layer. *Appl. Phys. Lett.* **2023**, *122* (21), 212101.
- (12) Yang, T.; Shou, C.; Almujtabi, A.; Tran, J.; Lin, Q.; Li, Y.; Mahmud, Q. S.; Wei, P.; Liu, J. Investigation of Phase Transition and Ultrawide Band Gap Engineering in MgGaO Semiconductor Thin Films. ACS Appl. Opt. Mater. 2023, 1 (10), 1670–1678.
- (13) Yang, T.; Shou, C.; Xu, L.; Tran, J.; He, Y.; Li, Y.; Wei, P.; Liu, J. Metal-Semiconductor-Metal Photodetectors Based on β -MgGaO Thin Films. *ACS Appl. Electron. Mater.* **2023**, 5 (4), 2122–2130.
- (14) Hou, Q.; Liu, K.; Han, D.; Zhu, Y.; Chen, X.; Li, B.; Liu, L.; Shen, D. MOCVD Growth of MgGa₂O₄ Thin Films for High-Performance Solar-Blind UV Photodetectors. *Appl. Phys. Lett.* **2022**, 120 (1), 011101.
- (15) Guo, Q.; Tetsuka, J.; Chen, Z.; Arita, M.; Saito, K.; Tanaka, T. Low Temperature Growth of MgGa₂O₄ Films for Deep Ultraviolet Photodetectors. *Opt. Mater.* **2023**, *143*, 114267.
- (16) Hou, Q.; Liu, K.; Chen, X.; Yang, J.; Ai, Q.; Cheng, Z.; Zhu, Y.; Li, B.; Liu, L.; Shen, D. Effects of Mg Component Ratio on Photodetection Performance of MgGa₂O₄ Solar-Blind Ultraviolet Photodetectors. physica status solidi (RRL) Rapid Research Letters 2022, 16 (8), 2200137.
- (17) Onuma, T.; Fujioka, S.; Yamaguchi, T.; Higashiwaki, M.; Sasaki, K.; Masui, T.; Honda, T. Correlation between Blue Luminescence Intensity and Resistivity in β -Ga₂O₃ Single Crystals. *Appl. Phys. Lett.* **2013**, *103* (4), 041910.
- (18) Wang, Y.; Dickens, P. T.; Varley, J. B.; Ni, X.; Lotubai, E.; Sprawls, S.; Liu, F.; Lordi, V.; Krishnamoorthy, S.; Blair, S.; Lynn, K. G.; Scarpulla, M.; Sensale-Rodriguez, B. Incident Wavelength and Polarization Dependence of Spectral Shifts in β -Ga₂O₃ UV Photoluminescence. *Sci. Rep* **2018**, 8 (1), 18075.
- (19) Islam, M. M.; Rana, D.; Hernandez, A.; Haseman, M.; Selim, F. A. Study of Trap Levels in β -Ga₂O₃ by Thermoluminescence Spectroscopy. *J. Appl. Phys.* **2019**, *125* (5), 055701.
- (20) Zhang, K.; Xu, Z.; Zhang, S.; Wang, H.; Cheng, H.; Hao, J.; Wu, J.; Fang, F. Raman and Photoluminescence Properties of Un-/Ion-Doped β -Ga₂O₃ Single-Crystals Prepared by Edge-Defined Film-Fed Growth Method. *Physica B: Condensed Matter* **2021**, 600, 412624.
- (21) Zhang, K.; Xu, Z.; Zhao, J.; Wang, H.; Hao, J.; Zhang, S.; Cheng, H.; Dong, B. Temperature-Dependent Raman and Photoluminescence of β -Ga₂O₃ Doped with Shallow Donors and Deep Acceptors Impurities. *J. Alloys Compd.* **2021**, 881, 160665.
- (22) Liu, Z.; Hu, P.; Jing, X.; Wang, L. Luminescence of Native Defects in MgGa₂O₄. J. Electrochem. Soc. **2009**, 156 (1), H43.
- (23) Mlotswa, D. V.; Noto, L. L.; Mofokeng, S. J.; Obodo, K. O.; Orante-Barrón, V. R.; Mothudi, B. M. Luminescence Dynamics of MgGa₂O₄ Prepared by Solution Combustion Synthesis. *Opt. Mater.* **2020**, *109*, 110134.
- (24) Akazawa, H.Formation of Various Phases of Gallium Oxide Films Depending on Substrate Planes and Deposition Gases. *Vacuum* **2016**, *123*, 8–16.
- (25) Ghose, S.; Rahman, S.; Hong, L.; Rojas-Ramirez, J. S.; Jin, H.; Park, K.; Klie, R.; Droopad, R. Growth and Characterization of β -Ga₂O₃ Thin Films by Molecular Beam Epitaxy for Deep-UV Photodetectors. *J. Appl. Phys.* **2017**, *122* (9), 095302.
- (26) Ema, K.; Sasaki, K.; Kuramata, A.; Murakami, H. Homo- and Hetero-Epitaxial Growth of β -Gallium Oxide via GaCl₃-O₂-N₂ System. *J. Cryst. Growth* **2021**, *564*, 126129.
- (27) Luchechko, A.; Kravets, O. Synthesis and Luminescent Properties of Magnesium Gallate Spinel Doped with Mn²⁺ and Eu³⁺ Ions. *physica status solidi c* **2017**, *14* (1–2), 1600146.
- (28) Suzuki, T.; Hughes, M.; Ohishi, Y. Optical Properties of Ni-Doped $MgGa_2O_4$ Single Crystals Grown by Floating Zone Method. *J. Lumin.* **2010**, *130* (1), 121–126.

- (29) Bi, X.; Wu, Z.; Huang, Y.; Tang, W. Stabilization and Enhanced Energy Gap by Mg Doping in ε -Phase Ga_2O_3 Thin Films. *AIP Advances* **2018**, 8 (2), 025008.
- (30) Wei, J.; Kim, K.; Liu, F.; Wang, P.; Zheng, X.; Chen, Z.; Wang, D.; Imran, A.; Rong, X.; Yang, X.; Xu, F.; Yang, J.; Shen, B.; Wang, X. β -Ga₂O₃Thin Film Grown on Sapphire Substrate by Plasma-Assisted Molecular Beam Epitaxy. *J. Semicond.* **2019**, *40* (1), 012802.
- (31) Bui, Q. C.; Largeau, L.; Morassi, M.; Jegenyes, N.; Mauguin, O.; Travers, L.; Lafosse, X.; Dupuis, C.; Harmand, J.-C.; Tchernycheva, M.; Gogneau, N. GaN/Ga₂O₃ Core/Shell Nanowires Growth: Towards High Response Gas Sensors. *Applied Sciences* **2019**, 9 (17), 3528.
- (32) Oshima, T.; Okuno, T.; Fujita, S. Ga₂O₃ Thin Film Growth on C-Plane Sapphire Substrates by Molecular Beam Epitaxy for Deep-Ultraviolet Photodetectors. *Jpn. J. Appl. Phys.* **2007**, *46* (11R), 7217. (33) Chen, Z.; Ge, K.; Meng, D.; Chen, X. Pure-Phase Ga₂O₃ Films

Were Deposited on Sapphire Substrates by Radio Frequency

Magnetron Sputtering. Mater. Lett. 2022, 320, 132385.

- (34) Tang, Y.; Deng, M.; Zhou, Z.; Xu, X.; Wang, J.; Liu, Q. Bi-Activated MgGa₂O₄ Phosphors with Rich Defect Energy Levels: Spectral Property and Optical Storage Applications. *Ceram. Int.* **2022**, 48 (13), 19141–19149.
- (35) Zhu, X.; Zhang, Y.-W.; Zhang, S.-N.; Huo, X.-Q.; Zhang, X.-H.; Li, Z.-Q. Defect Energy Levels in Monoclinic β -Ga₂O₃. *J. Lumin.* **2022**, 246, 118801.
- (36) Varley, J. B.; Janotti, A.; Franchini, C.; Van de Walle, C. G. Role of Self-Trapping in Luminescence and p-Type Conductivity of Wide-Band-Gap Oxides. *Phys. Rev. B* **2012**, *85* (8), 081109.
- (37) Ho, Q. D.; Frauenheim, T.; Deák, P. Origin of Photoluminescence in Ga₂O₃. *Phys. Rev. B* **2018**, 97 (11), 115163.
- (38) Frodason, Y. K.; Johansen, K. M.; Vines, L.; Varley, J. B. Self-Trapped Hole and Impurity-Related Broad Luminescence in β -Ga₂O₃. *J. Appl. Phys.* **2020**, *127* (7), 075701.
- (39) Cooke, J.; Ranga, P.; Jesenovec, J.; McCloy, J. S.; Krishnamoorthy, S.; Scarpulla, M. A.; Sensale-Rodriguez, B. Effect of Extended Defects on Photoluminescence of Gallium Oxide and Aluminum Gallium Oxide Epitaxial Films. *Sci. Rep* **2022**, *12* (1), 3243.
- (40) Ghadbeigi, L.; Cooke, J.; Dang, G. T.; Kawaharamura, T.; Yasuoka, T.; Sun, R.; Ranga, P.; Krishnamoorthy, S.; Scarpulla, M. A.; Sensale-Rodriguez, B. Optical Characterization of Gallium Oxide α and β Polymorph Thin-Films Grown on c-Plane Sapphire. *J. Electron. Mater.* **2021**, *50* (6), 2990–2998.
- (41) Wang, X.; Qiao, H.; Liu, T.; Song, F.; An, Z.; Xu, Y.; Zhang, L.; Shi, F. Ultraviolet Photoluminescence of β -Ga₂O₃ Microparticles Synthesized by Hydrothermal Method. *J. Mater. Sci. Mater. Electron* **2022**, 33 (16), 13040–13050.
- (42) Jangir, R.; Porwal, S.; Tiwari, P.; Rai, S. K.; Mondal, P.; Ganguli, T.; Oak, S. M.; Deb, S. K. Photoluminescence Study of β-Ga₂O₃ Nanostructures under Different Oxygen Pressure Conditions. *AIP Conf. Proc.* **2013**, *1512* (1), 212–213.
- (43) Vasyltsiv, V.; Kostyk, L.; Tsvetkova, O.; Lys, R.; Kushlyk, M.; Pavlyk, B.; Luchechko, A. Luminescence and Conductivity of β -Ga₂O₃ and β -Ga₂O₃: Mg Single Crystals. *Acta Physica Polonica: A* **2022**, *141* (4), 312.
- (44) Gake, T.; Kumagai, Y.; Oba, F. First-Principles Study of Self-Trapped Holes and Acceptor Impurities in Ga₂O₃ Polymorphs. *Phys. Rev. Mater.* **2019**, 3 (4), 044603.
- (45) Lyons, J. L.; Janotti, A.; Van de Walle, C. G. Effects of Hole Localization on Limiting P-Type Conductivity in Oxide and Nitride Semiconductors. *J. Appl. Phys.* **2014**, *115* (1), 012014.
- (46) Cui, J. B.; Thomas, M. A. Power Dependent Photoluminescence of ZnO. J. Appl. Phys. 2009, 106 (3), 033518.
- (47) Sabbar, A.; Madhusoodhanan, S.; Al-Kabi, S.; Dong, B.; Wang, J.; Atcitty, S.; Kaplar, R.; Ding, D.; Mantooth, A.; Yu, S.-Q.; Chen, Z. High Temperature and Power Dependent Photoluminescence Analysis on Commercial Lighting and Display LED Materials for Future Power Electronic Modules. Sci. Rep 2019, 9 (1), 16758.
- (48) Fonoberov, V. A.; Alim, K. A.; Balandin, A. A.; Xiu, F.; Liu, J. Photoluminescence Investigation of the Carrier Recombination

- Processes in ZnO Quantum Dots and Nanocrystals. *Phys. Rev. B* 2006, 73 (16), 165317.
- (49) Shibata, H. Negative Thermal Quenching Curves in Photoluminescence of Solids. *Ipn. J. Appl. Phys.* **1998**, 37 (2R), 550.
- (50) Wu, Y.; Li, J.; Ding, H.; Gao, Z.; Wu, Y.; Pan, N.; Wang, X. Negative Thermal Quenching of Photoluminescence in Annealed ZnO-Al₂O₃ Core-Shell Nanorods. *Phys. Chem. Chem. Phys.* **2015**, *17* (7), 5360–5365.